

This document is the Accepted Manuscript version of a Published Work that appeared in final form in Langmuir, copyright © American Chemical Society after peer review and technical editing by the publisher.

To access the final edited and published work see:

<https://dx.doi.org/10.1021/acs.langmuir.5b04622>

Co-Cu nanoparticles: synthesis by galvanic replacement and phase rearrangement during catalytic activation

Raquel Nafria,[†] Aziz Genç,[¶] Maria Ibáñez,[†] Jordi Arbiol,^{¶,§} Pilar Ramírez de la Piscina,[‡] Narcís Homs,^{,‡,‡} Andreu Cabot,^{*,‡,§}*

[†] Catalonia Institute for Energy Research, IREC, 08930 Sant Adrià del Besos, Spain

[¶] Institut Català de Nanociència i Nanotecnologia, ICN2, Campus de la UAB, 08193 Bellaterra, Spain

[§] Institució Catalana de Recerca i Estudis Avançats, ICREA, 08010 Barcelona, Spain

[‡] Departament de Química Inorgànica and Institut de Nanociència i Nanotecnologia, Universitat de Barcelona, 08028 Barcelona, Spain

KEYWORDS: catalysis, colloidal synthesis, bimetallic nanoparticles, Co-Cu catalysts, CO₂ hydrogenation

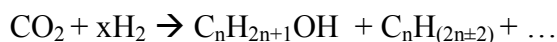
ABSTRACT: The control of the phase distribution in multicomponent nanomaterials is critical to optimize their catalytic performance. In this direction, while impressive advances have been achieved in the last decade in the synthesis of multicomponent nanoparticles and nanocomposites, element rearrangement during catalyst activation has been frequently overseen. Here, we present a facile galvanic replacement-based procedure to synthesize Co@Cu nanoparticles with narrow size and composition distributions. We further characterize their phase arrangement before and after catalytic activation. When oxidized at 350 °C in air to remove

1
2
3 organics, Co@Cu core-shell nanostructures oxidize to polycrystalline CuO-Co₃O₄ nanoparticles
4
5 with randomly distributed CuO and Co₃O₄ crystallites. During a posterior reduction treatment in
6
7 H₂ atmosphere, Cu precipitates in a metallic core and Co migrates to the nanoparticle surface to
8
9 form Cu@Co core-shell nanostructures. The catalytic behavior of such Cu@Co nanoparticles
10
11 supported on mesoporous silica was further analyzed toward CO₂ hydrogenation in real working
12
13 conditions.
14
15
16
17
18

19 1. INTRODUCTION

20
21
22 The rational design of more active, selective and durable catalysts requests for a deeper
23
24 fundamental understanding of the influence of each material parameter on its performance. This
25
26 ambitious goal requires engineering model catalysts with accurately tuned parameters and that
27
28 can be tested in real working conditions. The availability of such real model systems is critical to
29
30 overcome the material and pressure gaps partially disconnecting fundamental surface science
31
32 studies from real industrial catalysts.¹⁻⁴ In this framework, colloidal synthesis routes allow
33
34 producing large amounts of nanoparticles (NPs) with a unique control over composition, crystal
35
36 phase, particle size and surface facets.⁵⁻⁹ Such colloidal NPs can be supported on or assembled
37
38 into high surface area materials, and the resulting nanocomposites can be used as real catalytic
39
40 model systems to investigate the influence of material parameters in real reaction
41
42 conditions.^{2,4,10-12} This strategy is especially interesting in multi-metal catalysts, where not only
43
44 the parameters of each individual component, but also the distribution of these components, in
45
46 the form of independent entities, multi-metal alloys, Janus/dimer or core-shell NPs, have a
47
48 crucial role on the final catalytic performance.^{1-4,13}
49
50
51
52
53
54
55
56
57
58
59
60

1
2
3 A particularly interesting catalytic reaction involving multicomponent heterogeneous catalyst
4 and strongly influenced by the metal size and distribution is CO₂ hydrogenation:
5
6



7
8
9
10
11 The social and economic interest of CO₂ hydrogenation resides both on its potential to mitigate
12 CO₂ concentration in the atmosphere, and on the fact that CO₂ can be a feedstock of C₂₊
13 hydrocarbons and alcohols. Moreover CO₂ is a non-toxic, non-corrosive, and non-flammable
14 reactant, which can be easily stored and transported in liquid form under mild pressure.¹⁴⁻¹⁸
15
16
17
18
19

20
21 Among the numerous candidates for CO₂ hydrogenation, cobalt-copper catalysts are one of the
22 most selective and cost-effective option.¹⁹⁻²⁶ Joint effects of Co and Cu can be understood on the
23 basis of the properties of each single element catalyst. In the presence of H₂, Co is able to
24 dissociate CO and CO₂ and to hydrogenate the resulting surface carbon species into
25 hydrocarbons.^{27,28} Thus, it is used for the synthesis of medium chain and long-chain
26 hydrocarbons in the Fischer–Tropsch (FT) process.²⁹ On the other hand, Cu molecularly adsorbs
27 CO₂ and CO with a slow dissociation rate, which allows the incorporation of oxygen in the final
28 hydrogenated products, and thus the formation of alcohols.^{27,28,30} Therefore, Cu is used in the
29 synthesis of methanol from CO₂ hydrogenation or syngas.³¹⁻³⁴
30
31
32
33
34
35
36
37
38
39
40
41

42 Previous studies on the use of Cu or Co catalysts for CO₂ hydrogenation and FT reactions
43 demonstrated that parameters such as NP size strongly influence their performance. In particular,
44 cobalt activity decreased rapidly when the NP size was reduced below 10 nm, although no size
45 effect was observed on the selectivity.³⁵⁻³⁹ On the other hand, the turnover frequencies for
46 methanol formation from CO₂ hydrogenation of Cu NPs increased as NP size was reduced.⁴⁰
47
48 Beyond the properties of each individual catalytic material, the distribution of the active phases
49 is also key to determine the composition of the FT and CO₂ hydrogenation product stream. As an
50
51
52
53
54
55
56
57
58
59
60

1
2
3 example from the much better studied FT reaction, N. D. Subramanian et al. found that Co@Cu
4 core-shell NPs were more active than Co-Cu dimer NPs in the CO hydrogenation, but Co-Cu
5 NPs were more selective than Co@Cu NPs to the formation of ethanol and higher oxygenates.²⁷
6
7
8 Besides, G. Liu et al. reported that the hydrogenation of CO over Co@Cu NPs favored alcohol
9 synthesis, while Cu@Co NPs generated more hydrocarbons.²⁴ Recently, G. Prieto et al.
10 demonstrated that preventing the copper segregation on Co-Cu alloys increased the C₂₊ alcohols
11 selectivity in the FT process.⁴¹
12
13
14
15
16
17
18
19

20 While catalytic performance is extremely sensitive to surface composition of the catalyst, an
21 important challenge when dealing with multi-metallic NPs is the characterization and
22 understanding of the physical and chemical restructuring of the catalyst taking place during
23 activation treatments and catalytic test. This is particularly crucial in Co-Cu NPs and in general
24 in most transition metals, where activation/reduction processes inducing major chemical and
25 structural changes are absolutely necessary, and major structural and chemical changes can take
26 place during these processes as observed by Y. Xiang et al.,²⁵ S. Carencio et al.⁴² and S. Alayoglu
27 et al.²⁸. Nevertheless, due to the difficulties in producing catalysts with well-defined active phase
28 distribution, shape and size, the segregation and compositional re-organization of these
29 catalytically active phases during catalyst activation is frequently overseen.
30
31
32
33
34
35
36
37
38
39
40
41
42

43 We present here a new synthetic strategy to produce monodisperse Co-Cu NPs with controlled
44 metal ratios based on a galvanic replacement reaction. We used these NPs to gain understanding
45 on the structural and chemical changes taking place before and after the thermal treatments used
46 for the catalyst preparation and activation. We further analyze the catalytic behavior of these NPs
47 supported on mesoporous silica toward CO₂ hydrogenation.
48
49
50
51
52
53
54
55
56
57
58
59
60

2. EXPERIMENTAL

Chemicals: Cobalt carbonyl ($\text{Co}_2(\text{CO})_8$, $\geq 90\%$), copper(I) chloride (99.99%), copper (I) acetate (CuOAc , 97%), 1,2 anhydrous dichlorobenzene (DCB, 99%) and oleylamine (OLA, tech. 70%) were purchased from Sigma Aldrich. Trioctylphosphine oxide (TOPO, 99%) was purchased from Stream Chemicals, trioctylamine (TOA, 97%) from Acros, and tetradecylphosphonic acid (TDPA, 97%) from PlasmaChem GmbH. All products were used without further purification, except for OLA which was distilled. Analytical grade isopropanol, ethanol, hexane were purchased from Panreac. Stock solutions of copper (I) chloride in OLA (0.25 M) were prepared by dissolving 2.5 g of CuCl in 100 mL of OLA. All NP preparations were carried out using standard air-free techniques: a vacuum/dry-argon Schlenk line was used for the synthesis and an argon-filled glovebox for storing and handling air- and moisture-sensitive chemicals.

Cobalt nanoparticles: Co NPs were produced following a similar procedure as the one described previously by V. Puentes et al.,⁴³ but replacing oleic acid by OLA. In a typical synthesis, 0.1 g of TOPO, 15 mL of DCB and 0.3 mL of OLA were degassed in a 250 mL three-neck flask for 30 min in Ar. Then the solution was heated to 180 °C. At this temperature, 0.54 g of $\text{Co}_2(\text{CO})_8$ dissolved in 3 mL of DCB were rapidly injected. After 10 minutes, the solution was cooled down to room temperature. Co NPs were purified by multiple precipitation/re-dispersion steps using isopropanol as a non-solvent and hexane as solvent.

Copper nanoparticles: Cu NPs were prepared following the procedure reported by Yang et al.⁴⁴ In a typical synthesis, 10 mL of TOA was added in a 50 mL three-neck flask and heated to 130 °C for 30 min under Ar atmosphere. After cooling to room temperature, 0.246 g of CuOAc and 0.556 g of TDPA were placed into the flask. The mixture was heated up to 180 °C and

1
2
3 maintained at this temperature for 30 minutes. Afterward, the reaction temperature was further
4 increased to 270 °C and kept for another 30 minutes, before cooling down to ambient
5 temperature. Cu NPs were purified by multiple precipitation/re-dispersion steps using methanol
6 as a non-solvent and hexane as solvent.
7
8
9

10
11
12 ***Cobalt-copper nanoparticles:*** Co-Cu NPs were produced by a one-pot two-step procedure.
13 First, Co NPs were synthesized following the above procedure. In a second step, inside the 250
14 mL three-neck flask containing the Co NPs, different volumes of stock solution of Cu⁺ ions in
15 OLA (0.25 M) were added at room temperature (6.25 mL to produce Co_{0.6}-Cu_{0.4} NPs and 12.5
16 mL to get Co_{0.3}-Cu_{0.7} NPs). Then the mixture was heated up to 180 °C and maintained at this
17 temperature for 30 min. Afterward, the solution was cooled down and NPs were purified by three
18 hexane/isopropanol re-dispersion/precipitation cycles. NPs nomenclature (Co_x-Cu_y) indicates the
19 Co/Cu molar relation ([Co/Cu]=x/y).
20
21
22
23
24
25
26
27
28
29
30

31
32 ***SiO₂-supported nanoparticles:*** Metal NPs were incorporated via capillary inclusion to a
33 mesoporous hydrophobic SiO₂ support with a surface area of 191 m²/g and an average pore size
34 of 21 nm (AEROSIL R-9200 hydrophobic silica).^{28,45} In a typical preparation, 2 g of SiO₂ were
35 added to a hexane solution containing 200 mg of NPs (~ 150 mg NPs after ligand removal). The
36 slurry was sonicated for 2 h at room temperature to facilitate the introduction of NPs within the
37 silica pores. After that, hexane was evaporated under vacuum. Before catalyst characterization
38 and catalytic test, the nanopowder was annealed at 350 °C for 4h in air flow to remove organics.
39
40
41
42
43
44
45
46
47

48
49 ***Materials characterization:*** X-ray diffraction (XRD) patterns were obtained on a Bruker D8
50 automated diffractometer, equipped with a primary monochromator and a LynxEye detector and
51 using Cu K α radiation ($\lambda=1.5406$ Å). The instrument resolution was 0.05° in 2 θ , the studied
52 range was between 35–55° and the acquisition time for each sample was set to 2 h 20 min. Metal
53
54
55
56
57
58
59
60

1
2
3 contents were determined using optical emission spectroscopy by means of inductively coupled
4 plasma (ICP) on a Perkin Elmer Optima 3200 RL system. The specific surface area of the
5 materials was determined by N₂ adsorption at 77 K using a Tristar II 3020 Micromeritics system.
6
7 Thermogravimetric analyses (TGA) were performed in the temperature range of 30–700 °C at a
8 heating rate of 5 °C min⁻¹ under air using a Perkin Elmer TGA4000. Transmission electron
9 microscopy (TEM) and high resolution TEM (HRTEM) micrographs were obtained using a Carl
10 ZEISS LIBRA 120 microscope operated at 120 keV and a field emission gun (FEG) FEI Tecnai
11 F20 microscope operated at 200 keV, respectively. Scanning TEM (STEM)-electron energy-loss
12 spectroscopy (EELS) and STEM-energy dispersive X-ray spectroscopy (EDX) analyses are
13 conducted on the Tecnai microscope equipped with high angle annular dark field (HAADF) and
14 EDX detectors and a Quantum Gatan Image Filter (GIF). EDX analyses were performed with
15 an EDAX Octane T Ultra W /Apollo XLT2 SDD. The software used to interpret the images was
16 the FEI TEM Imaging & Analysis (TIA).
17
18
19
20
21
22
23
24
25
26
27
28
29
30
31
32
33

34 Hydrogen temperature-programmed reduction (TPR) was performed using a Micromeritics
35 AutoChem HP 2950 chemisorption analyzer. 50 mg of sample were pretreated at 90 °C for 30
36 min under flowing He (50 mL/min). After cooling to room temperature, the samples were
37 reduced in a flow of 12 vol% H₂/Ar (50 mL/min) and temperature was linearly increased at a rate
38 of 10 °C/min up to 800 °C.
39
40
41
42
43
44
45

46 The Cu⁰ surface area was determined by dissociative N₂O adsorption using a Micromeritics
47 AutoChem HP 2950 chemisorption analyzer. 50 mg of each sample were pretreated at 90 °C for
48 30 min under flowing He (50 mL/min). After cooling to room temperature, samples were
49 reduced in a flow of 12 vol% H₂/Ar (50 mL/min) and temperature was linearly increased at a rate
50 of 10 °C/min up to 350 °C at 30 bar. Again after cooling at 35 °C, samples were oxidized in a
51
52
53
54
55
56
57
58
59
60

1
2
3 flow of 6% N₂O/He (10 mL/min) for 1 hour. Finally, samples were flushed with He to remove
4 the oxidant and cooled to room temperature to start another TPR run. The exposed Cu surface
5 area (S_{Cu}) in the reduced catalysts was calculated on the basis of Cu/N₂O = 2 titration
6 stoichiometry and a surface atomic density of 1.4 × 10¹⁹ Cu atoms per m².
7
8
9

10
11
12 **Catalytic behavior:** Catalytic tests were carried out in a Microactivity-Reference unit (PID
13 Eng&TECH) in the temperature range 280–350 °C at 30 bar. 100 mg of catalyst was mixed with
14 inactive SiC (Prolabo, 0.5 mm) and placed in a tubular fixed-bed reactor (305 mm long, 9 mm
15 i.d., 316-L stainless steel) up to a catalytic bed volume of 1 mL. The temperature was measured
16 by a thermocouple in direct contact with the catalytic bed. Before the reaction, the catalyst was
17 in-situ reduced using a mixture of 12% vol/vol H₂/Ar, temperature and pressure were linearly
18 increased at 350 °C and 30 bar for 1 h and then kept at these conditions for another 30 minutes.
19
20 Thereafter, the pressure was kept at 30 bar and the temperature was decreased to 280 °C. Then
21 the catalyst was exposed to a reactant gas mixture of CO₂/H₂= 1/3 balanced with 20% of N₂, as
22 an internal standard, under a gas hourly space velocity (GHSV) of 3000 h⁻¹. After a period of 4 h
23 at 280 °C, the reaction temperature was consecutively increased to 300 °C, 320 °C, 340 °C and
24 350 °C and maintained at each temperature for 4 h. After each temperature change, the system
25 was stabilized for 1 h and then the corresponding initial activity at a given temperature was
26 determined. The products were analyzed on-line with a GC system (Varian 450-GC) equipped
27 with a methanizer, TCD and FID detectors. CO₂ conversion (X_{CO₂}) and the selectivity (S_i) for
28 each product (excluding H₂O) were calculated according to:
29
30
31
32
33
34
35
36
37
38
39
40
41
42
43
44
45
46
47
48
49
50
51
52

$$X_{CO_2} = \frac{\sum n_i P_i}{[CO_2] + \sum n_i P_i}$$

53
54
55
56
57
58
59
60

$$S_i = \frac{n_i P_i}{\sum n_i P_i}$$

where P_i and n_i are the molar concentration and the number of carbon atoms of a specific product in the outlet gas, and $[CO_2]$ is the CO_2 molar concentration in the outlet gas. The relative selectivities of the catalysts towards the formation of hydrogenated products were calculated as S_i , but excluding CO.

3. RESULTS AND DISCUSSION

Co-Cu NPs were produced by a one-pot two-step procedure. First, Co NPs were obtained by $Co(CO)_8$ decomposition in the presence of TOPO and OLA at 180 °C. After 10 min reaction, the solution was cooled down to room temperature and spherical Co NPs with an average size of 10 nm were obtained (Figure 1a). Then, Cu^+ ions were added to the Co NPs solution, and the mixture was heated up again to 180 °C. After 30 min reaction, slightly larger spherical NPs were obtained (Figure 1c). HRTEM micrographs showed the presence of Moiré fringes in the final Co-Cu NPs, pointing toward the superposition of two crystalline structures (Figure 1d). In the shell, the (011) and (111) planes of cuprite Cu_2O with 2.44 Å and 2.98 Å distances, could be evidenced. EELS elemental maps revealed the final Co-Cu NPs to be composed by a Co core and a partially oxidized Cu shell (Figure 1e), although a minor alloying cannot be discarded. The shell oxidation was associated with the NPs interaction with air during purification and during the preparation and transportation of TEM grids.

The Co core clearly shrank with the Cu^+ introduction, up to the point that when an excess amount of Cu^+ ions was introduced, Co was totally dissolved and pure Cu NPs were obtained. On the other hand, the injection of the Cu precursor in the exact same reaction conditions but in

1
2
3 the absence of Co NPs, did not result in the formation of Cu NPs. These experimental facts
4 evidenced that the Cu shell grew by the galvanic replacement of Co by Cu^+ ions in solution.⁴⁶
5
6 This replacement was driven by the larger reduction potential of Cu^+ compared with Co^{2+} (at 25
7
8 $^{\circ}\text{C}$ and 1 atm, $E^{\circ}(\text{Co}^{2+}/\text{Co}) = -0.28 \text{ V}$; $E^{\circ}(\text{Cu}^+/\text{Cu}) = 0.52 \text{ V}$). While galvanic replacement
9
10 generally results in the formation of porous structures, the relatively high reaction temperatures
11
12 used here ($180 \text{ }^{\circ}\text{C}$) could allow the formed vacancies to diffuse to the surface, thus finally
13
14 resulting in solid NPs. Because oxidation of each Co atom required the reduction and
15
16 incorporation of two Cu^+ ions, increasingly larger NPs were obtained when increasing the Cu-to-
17
18 Co ratio. Such a synthetic strategy allowed to carefully adjust the metal composition of the final
19
20 NPs and to produce Co-Cu NPs with the full range of Cu content by introducing the required
21
22 precise amounts of copper ions..
23
24
25
26
27
28

29 Owing to the core-shell nature of the Co-Cu NPs produced by the galvanic replacement
30 strategy, we refer to them using the nomenclature: $\text{Co}_x@\text{Cu}_{1-x}$, where x and $1-x$ respectively
31
32 denote the Co and Cu atomic ratio within the NP. We will maintain this nomenclature even after
33
34 thermal treatment of the NPs in oxidizing or reducing atmospheres, which, as detailed below,
35
36 clearly change the NP composition and phase distribution.
37
38
39

40
41 As a reference for the chemical, structural and functional characterization of the $\text{Co}@\text{Cu}$ NPs,
42
43 10 nm Co NPs were also prepared by the same procedure (1st step) and 10 nm spherical Cu NPs
44
45 were prepared following Yang et al.'s procedure (Figure 1b).⁴⁴
46
47
48
49
50
51
52
53
54
55
56
57
58
59
60

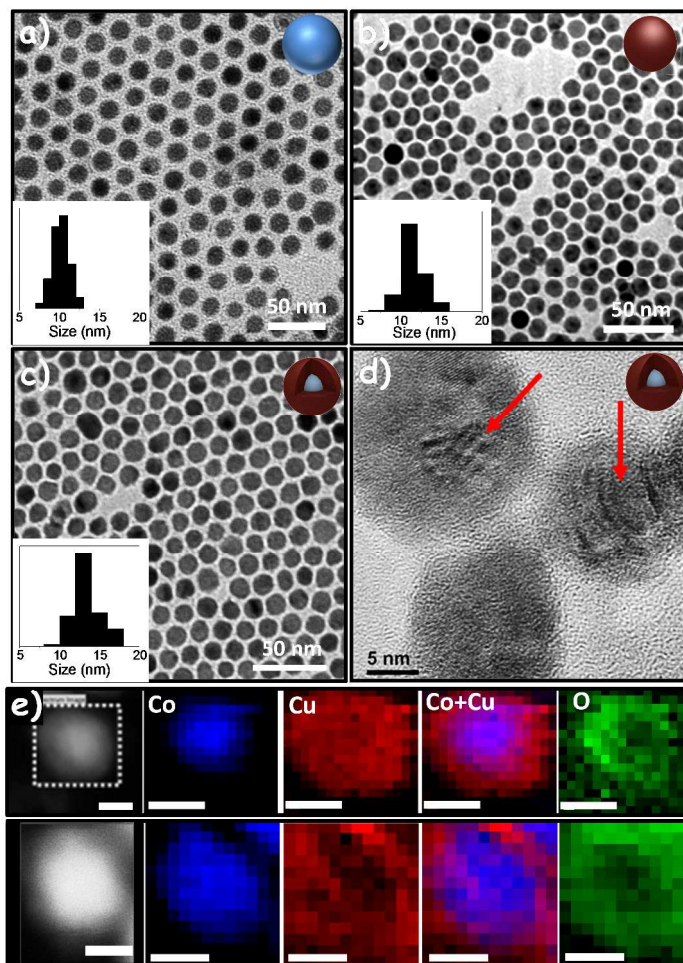


Figure 1. a)-c) TEM micrographs and size histograms (insets) of the Co (a), Cu (b) and Co_{0.6}@Cu_{0.4} (c) NPs. d) HRTEM micrograph of Co@Cu NPs. e) Two examples of HAADF (Z-contrast) images and Co, Cu and O EELS compositional maps of Co_{0.6}@Cu_{0.4} NPs. Scale bars correspond to 5 nm.

Figure 2 shows the XRD patterns of Co, Cu and two Co@Cu samples with different Co/Cu molar ratio: Co_{0.6}@Cu_{0.4} and Co_{0.3}@Cu_{0.7}. Co and Cu NPs crystallized in the ϵ -Co and face centered cubic (fcc, JCPDS 89-2838) phases, respectively.⁴⁷ However, Co@Cu NPs did not display the ϵ -Co phase, but showed a XRD pattern that resembled a fcc phase with lattice parameters in between those of Co and Cu fcc phases. We speculate that the metastable ϵ -Co

1
2
3
4
5
6
7
8
9
10
11
12
13
14
15
16
17
18
19
20
21
22
23
24
25
26
27
28
29
30
31
32
33
34
35
36
37
38
39
40
41
42
43
44
45
46
47
48
49
50
51
52
53
54
55
56
57
58
59
60

phase transformed to the stable Co_{fcc} during the additional 30 min treatment at 180 °C used to grow the Cu shell. A slight Co-Cu alloying could help in this direction, although the solubility of the two metals is very low in the temperature range here considered.^{28,42,48-50}

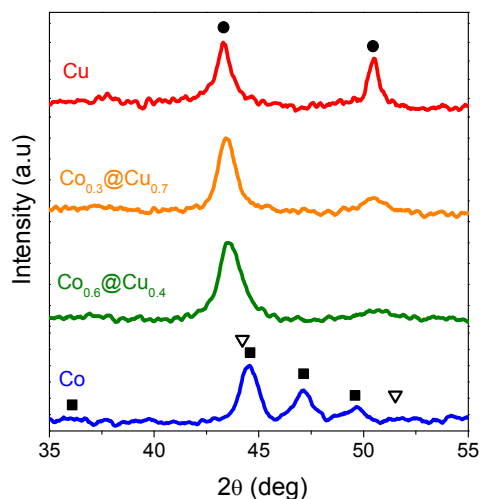


Figure 2. XRD patterns of Co, $\text{Co}_{0.6}@\text{Cu}_{0.4}$, $\text{Co}_{0.3}@\text{Cu}_{0.7}$ and Cu unsupported nanoparticles. Peaks corresponding to ■ ϵ -Co;⁴⁷ ▽ Co fcc (JCPDS 15-0806); and ● Cu fcc (JCPDS 89-2838) are marked as a reference.

Five model catalysts were prepared by capillary inclusion of colloidal NPs (7 %wt) into mesoporous hydrophobic SiO_2 : i) Co/ SiO_2 ; ii) Cu/ SiO_2 ; iii) Co/ SiO_2 +Cu/ SiO_2 physical mixture (50% wt); iv) $\text{Co}_{0.6}@\text{Cu}_{0.4}/\text{SiO}_2$; and v) $\text{Co}_{0.3}@\text{Cu}_{0.7}/\text{SiO}_2$. Organic capping agents from the NP surface were thermally decomposed in air for 4 h at 350 °C. This temperature was selected on the basis of TGA (supporting information, SI, Figure S11). The composition of the final catalysts, calculated by ICP, is displayed in Table S11.

Figure 3a shows a low magnification HAADF STEM micrograph of the $\text{Co}_{0.3}@\text{Cu}_{0.7}/\text{SiO}_2$ sample after thermal treatment in air. High contrast $\text{Co}_{0.3}@\text{Cu}_{0.7}$ NPs can be identified within the lower contrast SiO_2 matrix. While most NPs were found individually distributed over the SiO_2

1
2
3 surface, some aggregation was also observed. Because of this slight aggregation, we discarded
4
5 the Co+Cu/SiO₂ catalyst, with a mixture of Co and Cu NPs simultaneously incorporated in the
6
7 same support, as a reference material, as it contained an un-controlled combination of
8
9 independent Cu and Co NPs and aggregates of Co+Cu NPs.
10
11

12
13 HRTEM analysis (Figures 3b, SI2, SI3) showed the oxidized core-shell NPs to be
14
15 polycrystalline. Power spectrum analysis revealed the presence of the fcc Co₃O₄ and/or a Co₃₋
16
17 _xCu_xO₄ phase across the NP. Spinel cubic phase has a general formula AB₂O₄, where A and B
18
19 correspond to tetrahedral and octahedral cation sites, respectively, in a cubic close packing of
20
21 oxygen. Cu²⁺ may substitute Co³⁺ at octahedral sites and result in the Co_{3-x}Cu_xO₄ spinel phase.
22
23 While Co₃O₄ and Co_{3-x}Cu_xO₄ phases could not be differentiated due to their small lattice
24
25 parameter differences, the random distribution of phases and metals within each NP already
26
27 pointed toward the inter-diffusion of the two elements, Co and Cu, during oxidation at 350 °C.
28
29
30
31

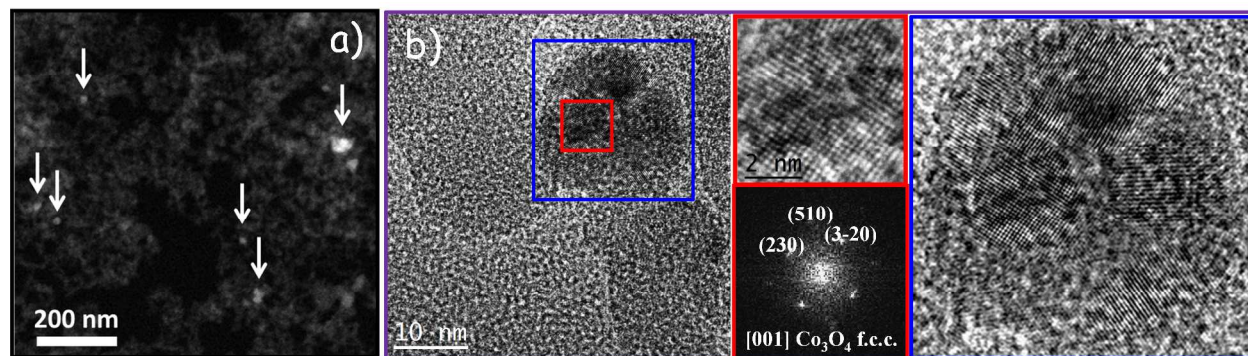


Figure 3. a) Low magnification HAADF-STEM micrograph of Co_{0.3}@Cu_{0.7}/SiO₂. Arrows point at the higher contrast Co@Cu NPs; b) HRTEM micrograph showing a polycrystalline oxidized Co_{0.3}@Cu_{0.7} NP. A detail of the blue region clearly shows the NP polycrystallinity. A detail of the red squared region and its corresponding power spectrum shows a Co₃O₄ or Co_{3-x}Cu_xO₄ fcc phase (space group = Fd3-ms) with lattice parameter a = 0.814 nm and visualized along its [001] zone axis.

The nature of the oxide phases formed after oxidation was further analyzed by XRD (Figure 4). In the monometallic catalysts, Co/SiO₂ and Cu/SiO₂, main diffraction peaks of Co₃O₄ spinel phase (JCPDS 42-1467) and CuO monoclinic phase (JCPDS 05-0661) were identified, respectively. The Co/SiO₂+Cu/SiO₂ catalyst showed the peaks corresponding to the same oxide phases detected in monometallic samples. In the Co@Cu/SiO₂ catalysts, XRD peaks corresponding to the CuO monoclinic phase were clearly identified. Furthermore, diffraction peaks at 31.2°, 36.7° and 44.7° could be assigned to the presence of Co₃O₄ and/or Co_{3-x}Cu_xO₄ in spinel phase. From the ratio between the CuO and the Co₃O₄ XRD peaks obtained from the 50 % Co/SiO₂+Cu/SiO₂ sample and considering 50 % of each CuO and Co₃O₄ in this material, we estimated the Co_{3-x}Cu_xO₄ spinel phase could account for up to a 10 % of the Cu atoms in the Co_{0.3}@Cu_{0.7}/SiO₂ and up to a 20 % of the Cu in the Co_{0.6}@Cu_{0.4}/SiO₂.

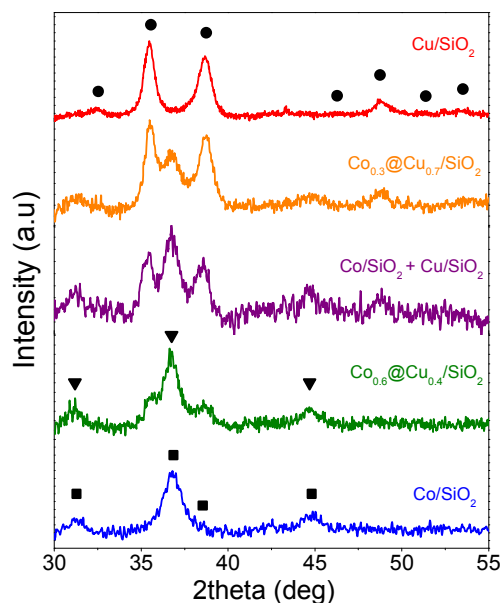


Figure 4. XRD patterns of the Co/SiO₂, Cu/SiO₂, Co/SiO₂+Cu/SiO₂, Co_{0.6}@Cu_{0.4}/SiO₂ and Co_{0.3}@Cu_{0.7}/SiO₂ catalysts after oxidation at 350 °C. The peaks corresponding to ■ Co₃O₄ (JCPDS 42-1467), ▼ Co₂CuO₄ (JCPDS 37-0878) and ● CuO (JCPDS 05-0661) are marked as a reference.

Figure 5 shows the TPR profiles measured from the different catalysts. The Co/SiO₂ catalyst was characterized by a two-step reduction profile with maxima of hydrogen consumption at 275 °C and 311 °C: Co₃O₄ → CoO → Co.⁵¹⁻⁵³ The reduction profile of Cu/SiO₂ was essentially characterized by a broad peak at lower temperatures than CoO, with a maximum of hydrogen consumption at 210 °C.^{53,54} The TPR profile of the Co/SiO₂+Cu/SiO₂ sample showed the peaks associated to the independent reduction of pure oxides, Co₃O₄ and CuO, what suggested no interaction or promotional effect between the two elements. On the other hand, Co@Cu/SiO₂ catalysts were characterized by a unique reduction peak at temperatures in between those of Co/SiO₂ and Cu/SiO₂ catalysts, which shifted toward lower temperatures when increasing the Cu content in the NP. This confirmed a synergistic effect in the reduction of both species, where Cu probably promoted the Coⁿ⁺ reduction, and suggested an intimate contact of the cobalt and copper species and a good sample homogeneity.⁵³⁻⁵⁶

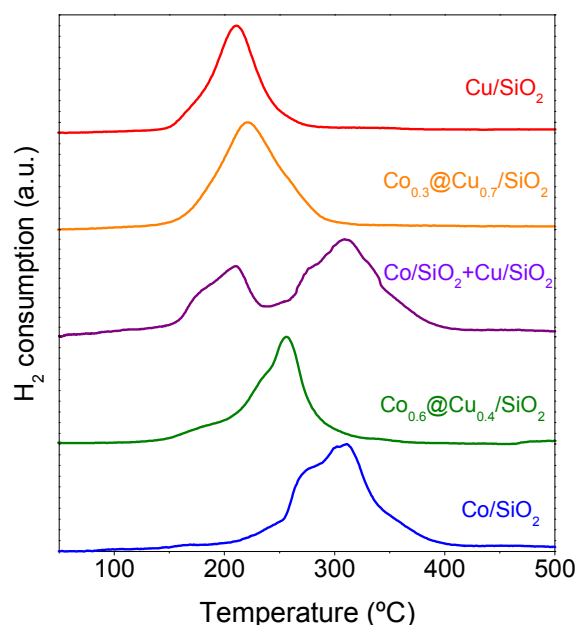
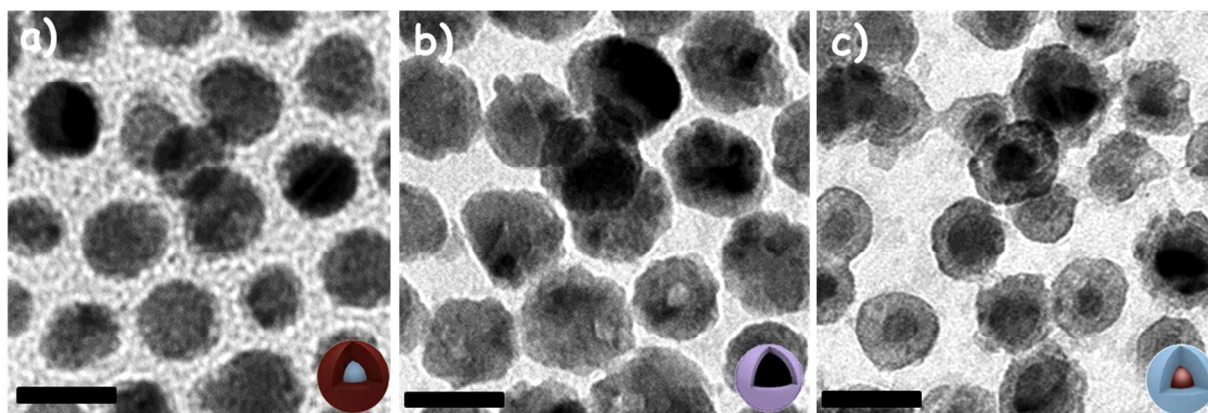


Figure 5. H₂ temperature programmed reduction profiles of Co/SiO₂, Cu/SiO₂, Co/SiO₂+Cu/SiO₂, Co_{0.6}@Cu_{0.4}/SiO₂ and Co_{0.3}@Cu_{0.7}/SiO₂ catalysts.

1
2
3 To further study the structural and chemical evolution of the Co@Cu NPs during oxidation and
4 reduction treatments, TEM analysis of the NPs supported on a silicon nitride grid was carried out
5 after each thermal treatment. Figure 6 shows TEM micrographs of the exact same $\text{Co}_{0.3}\text{@Cu}_{0.7}$
6 NPs just after their preparation (Figure 6a), after oxidation at 350 °C for 4 hours in air (Figure
7 6b) and after reduction at 350 °C and 30 bar in a 12 % H_2 -Ar (Figure 6c). After the thermal
8 treatment in air, slightly larger polycrystalline NPs with no clear contrast between a hypothetical
9 core and a shell were identified. Some voids were observed within the NPs after oxidation,
10 which we assigned to the nanoscale Kirkendall effect and pointed toward a faster diffusion of Co
11 and/or Cu than oxygen through the growing metal oxide shell (Figure SI4).⁵⁷⁻⁶⁰
12
13
14
15
16
17
18
19
20
21
22
23
24

25 After the reduction treatment, NPs shrank and a core-shell structure was recovered. HRTEM
26 and EDS analysis showed the reduced NPs to be formed by a polycrystalline CoO shell and a
27 metallic Cu core (Figure 7, SI5-SI7). Taking into account the hydrogen consumed from TPR
28 results, we believe that the cobalt oxide shell was completely reduced during the H_2 treatment,
29 but it oxidized when exposed to air before TEM analysis.
30
31
32
33
34
35
36



50
51 **Figure 6.** TEM micrographs from the same $\text{Co}_{0.3}\text{@Cu}_{0.7}$ NPs supported on a SiN_x TEM grid
52 after different treatments: a) initial $\text{Co}_{0.3}\text{@Cu}_{0.7}$ NPs, b) after thermal treatment in air at 350 °C
53 during 4h; c) after reduction in 12 % H_2 -Ar at 350 °C at 30 bar. Scale bar corresponds to 20 nm.
54
55
56
57
58
59
60

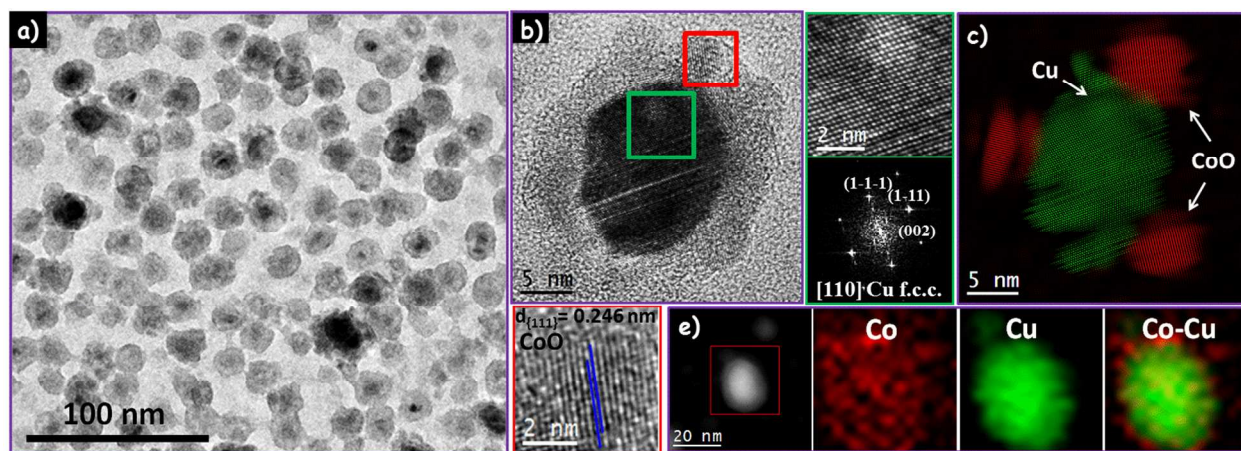


Figure 7. a) TEM micrographs of $\text{Co}_{0.3}@\text{Cu}_{0.7}$ NPs oxidized in air at 350 °C during 4h and reduced in 12 % $\text{H}_2\text{-Ar}$ at 350 °C at 30 bar; b) HRTEM micrograph of a reduced $\text{Co}_{0.3}@\text{Cu}_{0.7}$ NPs with details of shell (red squared) and core (green squared) regions and corresponding power spectrum of the core. HRTEM is consistent with a metallic Cu core and a CoO shell. c) Colorful crystallographic map of the same NP where green indicates the f.c.c. Cu phase and red indicates the f.c.c. CoO phase. e) EDX compositional maps of a $\text{Co}_{0.3}@\text{Cu}_{0.7}$ NP after the reduction process.

According to these experimental evidences, we hypothesize that during the oxidation treatment, the diffusion of cobalt through an initially formed CuO shell takes place, leaving a void within the particle. With the reduction treatment, metal copper collapsed to the center of the NP and Co remained at its surface. Upon exposure to air during TEM sample preparation and transportation, Co was oxidized into a thicker and lower contrast CoO shell than that of the initial $\text{Co}@\text{Cu}$ NPs. This explains the different electron microscopy contrast between the as-produced $\text{Co}@\text{Cu}$ NPs and the reduced ones. Notice finally that, in spite of the diffusion of the different components within each individual particle, resulting in an inversion of the core-shell structure, NPs supported on SiN_x did not coalesce or aggregate. These results are slightly different from those obtained by Somorjai and collaborators, who studied the compositional re-

1
2
3 organization of Cu@Co NPs, observing the surface segregation of Cu during oxidation, the
4 surface segregation of Co during reduction, and the formation Cu-Co dimers after the redox
5 conditioning.²⁸
6
7
8
9

10 The specific Cu⁰ surface area in the reduced catalysts was estimated by adsorptive
11 decomposition of nitrous oxide.^{61,62} We assumed the dissociation of nitrous oxide to take place
12 only on the surface of copper according to the reaction: $2\text{Cu}_{(s)} + \text{N}_2\text{O} \rightarrow \text{Cu}_2\text{O}_{(s)} + \text{N}_2$. The amount
13 of Cu₂O formed after N₂O chemisorption was determined using TPR. While it was previously
14 established that the optimum temperature range for N₂O adsorption was 60-90 °C,⁶¹⁻⁶³ our
15 reference Co/SiO₂ sample was also oxidized by N₂O in this temperature range. Therefore, to
16 selectively estimate the Cu surface area, we reduced the adsorption temperature to 35 °C, where
17 we measured an N₂O-related oxidation of the Cu/SiO₂ sample but not of the Co/SiO₂ catalyst.
18 Even in this low temperature range, Cu surface areas were overestimated (table SI2).
19 Nevertheless, they were systematically higher for catalyst with the following compositions
20 Cu/SiO₂ > Co_{0.3}@Cu_{0.7}/SiO₂ > Co_{0.6}@Cu_{0.4}/SiO₂ > Co/SiO₂ + Cu/SiO₂. These results may indicate
21 that in spite of the core-shell inversion, a significant part of the Cu surface areas were still
22 accessible within Co_{0.6}@Cu_{0.4}/SiO₂ and Co_{0.3}@Cu_{0.7}/SiO₂ catalysts. This suggests that the Co-
23 based shell was porous and permeable to N₂O or that the surface composition of the Co@Cu NPs
24 after reduction was not pure Co but a Co-Cu alloy which interacted with N₂O. However, N₂O
25 absorption results could be also explained by considering that the presence of a Cu core in direct
26 contact with the Co shell was able to promote Co oxidation by N₂O, although independent Co
27 NPs did not interact with N₂O at 35°C.
28
29
30
31
32
33
34
35
36
37
38
39
40
41
42
43
44
45
46
47
48
49
50
51
52

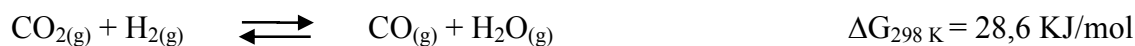
53 Figure 8 displays the total CO₂ hydrogenation conversion at 30 bar and 3000 h⁻¹ over SiO₂-
54 supported monometallic and bimetallic catalysts. Total conversions were much higher for the
55
56
57
58
59
60

1
2
3 two reference catalysts containing independent Co NPs than for the pure Cu-based catalyst and
4 the Co@Cu/SiO₂ catalysts. Previous works demonstrated that too small Co NPs (<10 nm)
5 showed lower activity in CO₂ hydrogenation^{28, 35-37} and F-T^{12,36,39} reactions and attributed it to a
6 higher susceptibility to oxidation^{11d} and a related lower capability to dissociate CO.³⁹ We
7 associate the higher CO₂ conversions of Co/SiO₂-containing catalysts to: i) the higher CO₂ and
8 CO dissociation rates on Co than Cu,^{64,65} ii) the larger size of the Co crystalline domains in the
9 Co/SiO₂ catalysts compared with the Co@Cu/SiO₂ catalysts; iii) the lower CO₂ hydrogenation
10 activity of the Co shells in Co@Cu/SiO₂ catalysts, which could also be related to a higher
11 oxidation susceptibility.
12
13
14
15
16
17
18
19
20
21
22
23

24 For all catalysts, conversion increased with temperature up to 340 °C. Above this temperature,
25 catalysts containing Co NPs showed a clear decrease in conversion (Figure 8). This is related to a
26 progressive loss of their capacity to produce hydrocarbons when heated at 340 °C and above
27 under reaction conditions (Figures SI8 and SI9). On the other hand, the conversion of the
28 Cu/SiO₂ and Co@Cu/SiO₂ catalysts was significantly more stable over time (Figures SI10-SI12).
29
30
31
32
33

34 CO, CH₄, C₂H₆, C₂H₄, C₃H₆, and traces of CH₃OH were the products obtained from the CO₂
35 hydrogenation reaction over all the catalysts. Nevertheless, each catalyst was characterized by
36 significantly different selectivities to each of these products. The main CO₂ hydrogenation
37 product on Co/SiO₂ was CH₄, with conversion selectivities up to a 70 % (Figure 8a). This result
38 is consistent with previous works showing that low space velocities and high pressures favored
39 high selectivities to methane on groups 8, 9 and 10 metals supported on SiO₂.^{66,67} Furthermore,
40 Co is known to adsorb CO and CO₂ dissociatively in the presence of H₂, leading to the loss of
41 oxygen as water and the production of oxygen free hydrocarbons. In this catalyst, CO
42 selectivities were in the range between 20% and 40% and increased with temperature in the high
43
44
45
46
47
48
49
50
51
52
53
54
55
56
57
58
59
60

temperature range measured as the reverse water gas-shift reaction (RWGS) reaction was favored:^{14,15,30}



The main reaction product of CO₂ hydrogenation on Cu/SiO₂ catalyst was CO, with selectivities up to 85 % (Figure 8b). CH₄ was a minor component in the product stream for this catalyst, with selectivities around 10 %. This is consistent with the molecular adsorption of CO₂ and CO on Cu and their slow dissociation, what favors alcohol production when combined with the appropriate support.^{30,31-34,68-72}

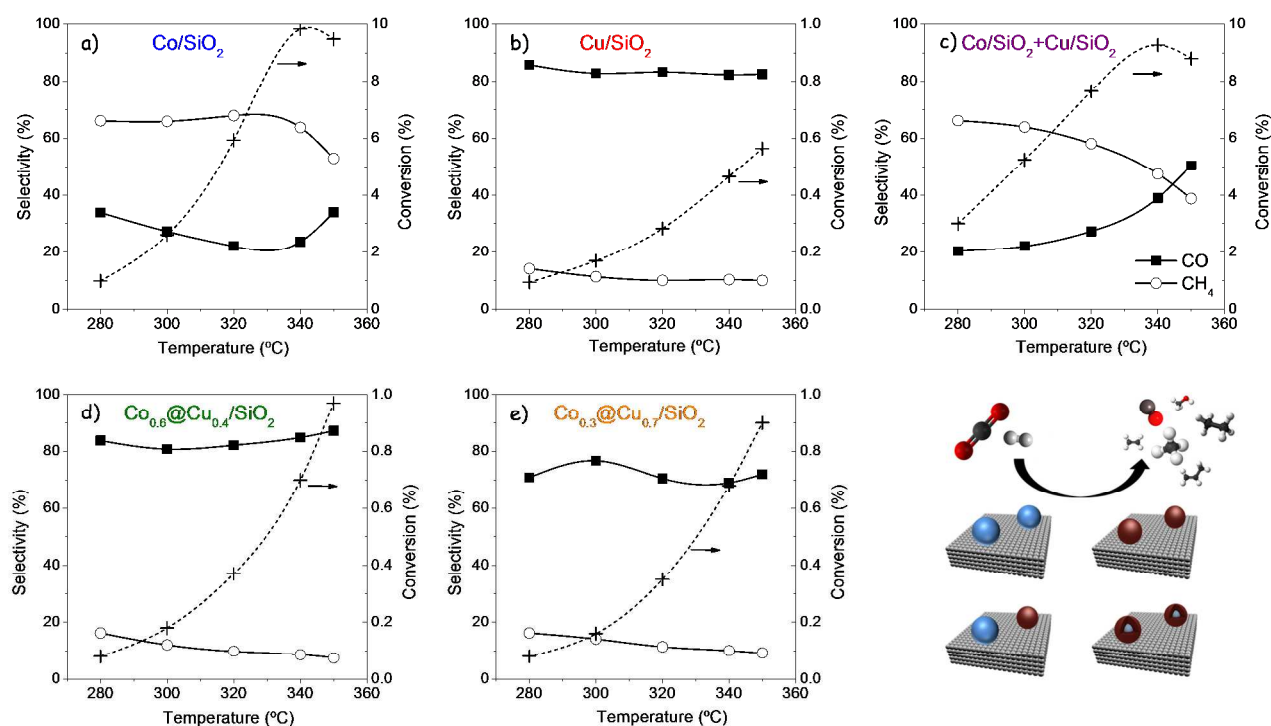


Figure 8. CO₂ conversion and selectivities to CO and CH₄ obtained from Co/SiO₂ (a), Cu/SiO₂ (b), Co/SiO₂+Cu/SiO₂ (c), Co_{0.6}@Cu_{0.4}/SiO₂ (d) and Co_{0.3}@Cu_{0.7}/SiO₂ (e) catalysts.

The catalytic performance of the physical mixture Co/SiO₂+Cu/SiO₂ was in between that of Co/SiO₂ and Cu/SiO₂, with CH₄ selectivities from 65 % to 40 % and CO selectivities in the range 20-50 % (Figure 8c). On the contrary, Co@Cu/SiO₂ catalysts showed much higher tendencies to

1
2
3 produce CO, as the Cu/SiO₂ catalyst, and were characterized by relatively low methane
4
5 selectivities (Figures 8d and 8e).
6

7
8 Aside from CO and CH₄, C₂ and C₃ products were also produced with significant rates over
9
10 monometallic and bimetallic catalysts. The production of higher hydrocarbons requires avoiding
11
12 the formation of CH₄, as it is the thermodynamically most stable product. To compare the
13
14 selectivity towards the formation of the different hydrogenated products, figure 9 displays the
15
16 relative selectivities (excluding CO) of the different catalysts towards the formation of methane,
17
18 ethane, ethylene, propene, and methanol.
19
20

21
22 The relative selectivities to C₂ compounds, ethane and ethylene, were much higher for
23
24 Cu/SiO₂ and Co@Cu/SiO₂ than for Co/SiO₂ and Co/SiO₂+Cu/SiO₂ catalysts. 40-65 % relative
25
26 selectivities toward the formation of C₂ products were obtained for Co@Cu/SiO₂ catalysts above
27
28 300 °C. Furthermore, propene was only detected on the bimetallic catalysts, with much higher
29
30 selectivities for the Co@Cu/SiO₂ than for Co/SiO₂+Cu/SiO₂ catalysts. The higher relative
31
32 selectivities of Co@Cu/SiO₂ catalysts to carbon chain growth confirmed the positive synergy
33
34 between the two metals when combined within the same particle.
35
36
37

38
39 Methanol selectivities were very low for all catalysts (Figure 9). We associate this
40
41 experimental fact to the need for a more suitable support than silica.⁷² It is generally accepted
42
43 that Cu is the active phase for methanol formation.^{30,31-34,68-72} However the support plays an
44
45 extremely important role, and oxide supports such as ZnO, ZrO₂ or Al₂O₃ have been found
46
47 essential to promote the methanol formation. As expected, Cu-containing catalyst showed much
48
49 higher relative methanol selectivities than Co/SiO₂. Furthermore, Co@Cu/SiO₂ catalysts also
50
51 showed relative selectivities to methanol well beyond those of Co/SiO₂+Cu/SiO₂ catalyst (Figure
52
53
54
55
56
57
58
59
60
9).

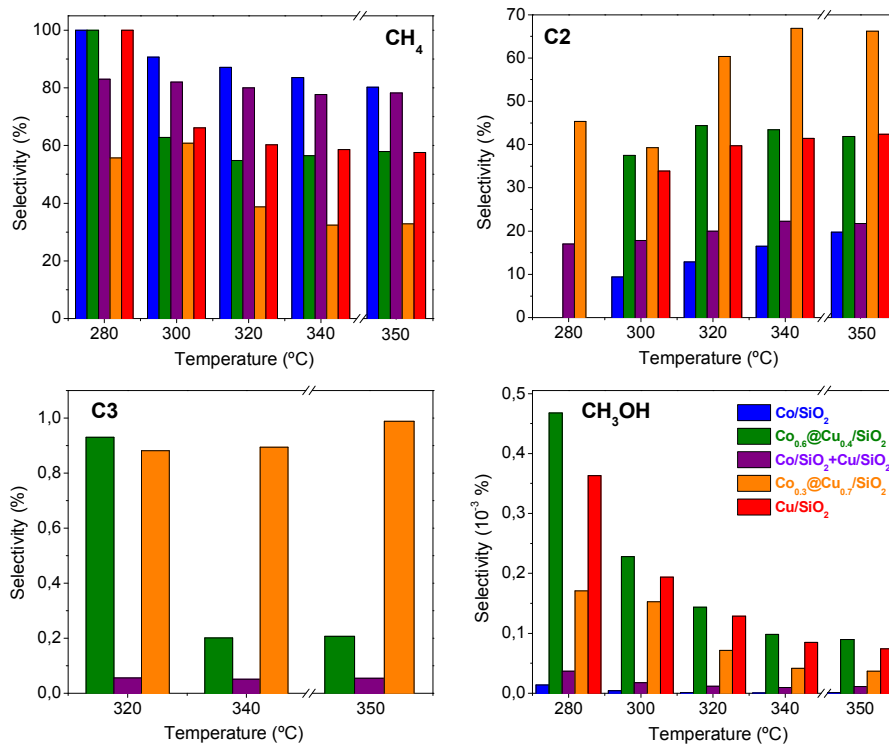


Figure 9. Relative selectivities related to hydrogenated products obtained from the Co/SiO₂, Cu/SiO₂, Co/SiO₂+Cu/SiO₂, Co_{0.6}@Cu_{0.4}/SiO₂ and Co_{0.3}@Cu_{0.7}/SiO₂ catalysts.

Catalysts were further analyzed after reaction. Figure 10a shows the XRD patterns of the initial Co_{0.3}@Cu_{0.7} NPs and of the Co_{0.3}@Cu_{0.7}/SiO₂ catalyst after the reduction treatment and after catalytic test. Notice that the cubic structure of the NPs was conserved. The narrower peaks after reduction and after reaction are related to a better crystallinity of the material after thermal treatment of the sample at 350 °C and under 30 bar of pressure. On the other hand, single particle compositional analysis of the Co_{0.3}@Cu_{0.7} NPs supported on a silicon nitrate TEM grid and exposed to the oxidation, reduction and reaction conditions showed the core-shell structure not to stand the reaction conditions. During reaction conditions, the two metal phases separated to form non-symmetric bimetallic heterostructures (Figure 10b).

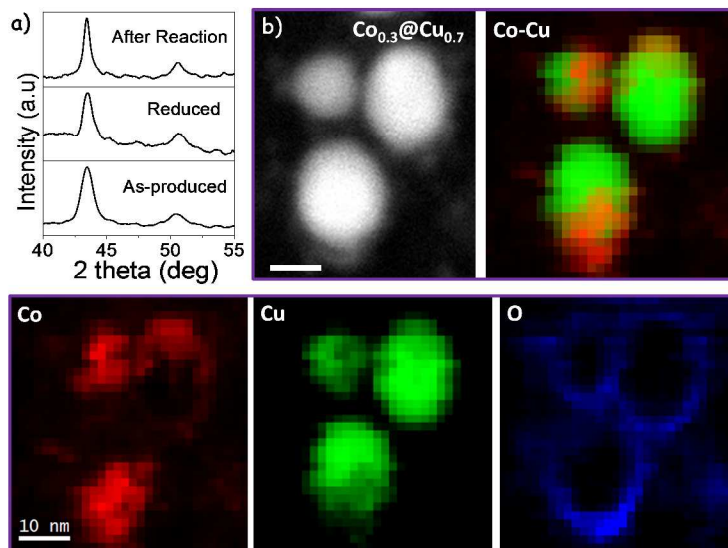


Figure 10. a) XRD patterns of the initial $\text{Co}_{0.3}\text{@Cu}_{0.7}$ NPs and of the $\text{Co}_{0.3}\text{@Cu}_{0.7}/\text{SiO}_2$ catalyst after the reduction treatment and after the catalytic test. B) HAADF-STEM micrograph and EELS chemical composition maps, Co (red), Cu (green) and O (blue), of three $\text{Co}_{0.3}\text{@Cu}_{0.7}$ NPs supported on a silicon nitride TEM grid and exposed to the consecutive, oxidation, reduction and reaction conditions. Scale bar = 10 nm

4. CONCLUSIONS

A new colloidal synthesis route to produce Co-Cu NPs with controlled composition based on the galvanic replacement of Co by Cu was detailed. This synthetic strategy allowed the preparation of Co-Cu model catalysts with well controlled parameters to be studied in real working conditions. These catalysts were thoroughly characterized to understand the interactions originated at the nanoscale between the two metals. TPR profiles showed a synergistic effect on the reduction of cobalt and copper in Co-Cu/SiO₂ catalysts. During oxidation and posterior reduction, a core-shell inversion was observed without coalescence or aggregation of the nanoparticles. We believe Co intermixed with Cu during the oxidation process and Cu reduced to

1
2
3 the center of the NP during the reduction treatment, while Co migrated at its surface.
4
5 Nevertheless, N₂O chemisorption pointed out the accessibility of the copper within the reversed
6
7 Co-Cu core-shell NPs. CO₂ conversion tests showed that catalysts containing large and pure Co
8
9 NPs were characterized by one order of magnitude higher total conversions. Nevertheless, a clear
10
11 synergism between Co and Cu was shown by the different TPR profiles and catalytic behavior in
12
13 CO₂ hydrogenation; Co-Cu/SiO₂ showed a better stability and higher relative selectivities to form
14
15 C-C bonds and methanol than monometallic catalysts and the physical mixture
16
17 Co/SiO₂+Cu/SiO₂. A more appropriate support than SiO₂ and possibly larger Co domains would
18
19 be necessary to improve both the total CO₂ conversion and the selectivity towards high
20
21 hydrocarbons and especially alcohols.
22
23
24
25
26
27
28

29 AUTHOR INFORMATION

30 31 **Corresponding Author**

32
33 *E-mail: narcis.homs@qi.ub.es

34
35 *E-mail: acabot@irec.cat

36 37 **Author Contributions**

38
39 The manuscript was written through contributions of all authors. All authors have given approval
40
41 to the final version of the manuscript.
42
43
44
45
46
47

48 ACKNOWLEDGMENT

49
50 The research was supported by the European Regional Development Funds and the Spanish
51
52 MICINN projects CSD2009-00050, MAT2014-52416-P and ENE2013-46624-C4-3-R. MI
53
54 thanks AGAUR for her Beatriu de Pinós postdoctoral grant 2013 BP-A00344. JA and AG
55
56
57
58
59
60

1
2
3 acknowledge the funding from the Spanish MINECO Severo Ochoa Excellence Program and
4
5 Generalitat de Catalunya 2014SGR1638.
6
7

8
9
10 ASSOCIATED CONTENT

11
12
13 **Supporting Information.** ICP metal contents, Cu surface areas, thermogravimetry results,
14 additional TEM and HRTEM micrograph, x-ray photoelectron spectroscopy (XPS) analysis of
15 the material after reaction and time evolution of total CO₂ conversions. This material is available
16 free of charge via the Internet at <http://pubs.acs.org>.
17
18
19
20
21
22

23
24
25
26 REFERENCES

- 27
28 (1) Somorjai, G. A.; Park, J. Y. Molecular Factors of Catalytic Selectivity. *Angew. Chem., Int.*
29 *Ed.* **2008**, *47*, 9212-9228.
30
31
32 (2) Jia, C. J.; Schüth, F. Colloidal Metal Nanoparticles as a Component of Designed Catalyst.
33 *Phys. Chem. Chem. Phys.* **2011**, *13*, 2457-2487.
34
35
36 (3) Zaera, F. Nanostructured Materials for Applications in Heterogeneous Catalysis.
37 *Chem. Soc. Rev.* **2013**, *42*, 2746-2762.
38
39
40 (4) Gross, E.; Somorjai, G. A. Molecular Catalysis Science: Nanoparticle Synthesis and
41 Instrument Development for Studies Under Reaction Conditions. *J. Catal.* **2015**, *328*, 91-
42 101.
43
44
45 (5) Yin, Y.; Alivisatos, A. P. Colloidal Nanocrystal Synthesis and the Organic–Inorganic
46 Interface. *Nature* **2005**, *437*, 664-670.
47
48
49
50
51
52
53
54
55
56
57
58
59
60

- 1
2
3
4
5
6
7
8
9
10
11
12
13
14
15
16
17
18
19
20
21
22
23
24
25
26
27
28
29
30
31
32
33
34
35
36
37
38
39
40
41
42
43
44
45
46
47
48
49
50
51
52
53
54
55
56
57
58
59
60
- (6) Luo, Z.; Ibáñez, M.; Antolín, A. M.; Genç, A.; Shavel, A.; Contreras, S.; Medina, F.; Arbiol, J.; Cabot, A. Size and Aspect Ratio Control of Pd₂Sn Nanorods and Their Water Denitration Properties. *Langmuir* **2015**, *31*, 3952-3957.
- (7) Yu, X.; Shavel, A.; An, X.; Luo, Z.; Ibáñez, M.; Cabot, A. The Effect of the Ga Content on the Photocatalytic Hydrogen Evolution of CuIn_{1-x}Ga_xS₂ Nanocrystals. *J. Am. Chem. Soc.* **2014**, *136*, 9236-9239.
- (8) Ibáñez, M.; Cabot, A. All Change for Nanocrystals. *Science* **2013**, *340*, 935-936.
- (9) Kovalenko, M.V. et al. Prospects of Nanoscience with Nanocrystals. *ACS Nano* **2015**, *9*, 1012-1057.
- (10) Nafria, R.; de la Piscina, P. R.; Homs, N.; Morante, J. R.; Cabot, A.; Diaz, U.; Corma, A. Embedding Catalytic Nanoparticles Inside Mesoporous Structures with Controlled Porosity: Au@TiO₂. *J. Mater. Chem. A* **2013**, *1*, 14170-14176.
- (11) Flox, C.; Rubio-Garcia, J.; Nafria, R.; Zamani, R.; Skoumal, M.; Andreu, T.; Arbiol, J.; Cabot, A.; Morante, J. R. Active Nano-CuPt₃ Electrocatalyst Supported on Graphene for Enhancing Reactions at the Cathode in all-Vanadium Redox Flow Batteries. *Carbon* **2012**, *50*, 2372-2374.
- (12) Herranz, T.; Deng, X.; Cabot, A.; Guo, J.; Salmeron, M. Influence of the Cobalt Particle Size in the CO Hydrogenation Reaction Studied by in Situ X-Ray Absorption Spectroscopy. *J. Phys. Chem. B* **2009**, *113*, 10721-10727.
- (13) Kwangjin, A.; Somorjai, G. A. Nanocatalysis I: Synthesis of Metal and Bimetallic Nanoparticles and Porous Oxides and Their Catalytic Reaction Studies. *Catal. Lett.* **2015**, *145*, 233-248.

- 1
2
3
4
5
6
7
8
9
10
11
12
13
14
15
16
17
18
19
20
21
22
23
24
25
26
27
28
29
30
31
32
33
34
35
36
37
38
39
40
41
42
43
44
45
46
47
48
49
50
51
52
53
54
55
56
57
58
59
60
- (14) Wang, W.; Wang, S.; Ma, X.; Gong, J. Recent Advances in Catalytic Hydrogenation of Carbon Dioxide. *Chem. Soc. Rev.* **2011**, *40*, 3703-3727.
- (15) Homs, N.; Toyir, J.; de la Piscina, P. R. Catalytic Processes for Activation of CO₂. *New and future Developments in Catalysis* Elsevier, **2013**.
- (16) Centi, G.; Perathoner, S. Opportunities and Prospects in the Chemical Recycling of Carbon Dioxide to Fuels. *Catal. Today* **2009**, *148*, 191-205.
- (17) Ma, J.; Sun, N.; Zhang, X.; Zhao, N.; Xiao, F.; Wei, W.; Sun, Y. A Short Review of Catalysis for CO₂ Conversion. *Catal. Today* **2009**, *148*, 221-231.
- (18) Nieskens, D. L.; Ferrari, D.; Liu, Y.; Kolonko, R. The Conversion of Carbon Dioxide and Hydrogen into Methanol and Higher Alcohols. *Catal. Commun.* **2011**, *14*, 111-113.
- (19) Courty, P.; Durand, D.; Freund, E.; Sugier, A. C₁-C₆ Alcohols From Synthesis Gas on Copper-Cobalt Catalysts. *J. Mol. Catal.* **1982**, *17*, 241-254.
- (20) Dalmon, J. A.; Chaumette, P.; Mirodatos, C. Higher Alcohols Synthesis on Cobalt Based Model Catalysts. *Catal. Today* **1992**, *15*, 101-127.
- (21) Mouaddib, N.; Perrichon, V.; Martin, G. A. Characterization of Copper-Cobalt Catalysts for Alcohol Synthesis from Syngas. *Appl. Catal. A* **1994**, *118*, 63-72.
- (22) Bailliard-Letournel, R. M.; Cobo, A. J. G.; Mirodatos, C.; Primet, M.; Dalmon, J. A. About the Nature of the Co-Cu Interaction in Co-Based Catalysts for Higher Alcohols Synthesis. *Catal. Lett.* **1989**, *2*, 149-156.
- (23) Cao, R.; Pan, W. X.; Griffin, G. L. Direct Synthesis of Higher Alcohols Using Bimetallic Copper/Cobalt Catalysts. *Langmuir* **1988**, *4*, 1108-1112.

- 1
2
3
4
5
6
7
8
9
10
11
12
13
14
15
16
17
18
19
20
21
22
23
24
25
26
27
28
29
30
31
32
33
34
35
36
37
38
39
40
41
42
43
44
45
46
47
48
49
50
51
52
53
54
55
56
57
58
59
60
- (24) Liu, G.; Niu, T.; Pan, D.; Liu, F.; Liu, Y. Preparation of Bimetal Cu–Co Nanoparticles Supported on Meso–Macroporous SiO₂ and Their Application to Higher Alcohols Synthesis from Syngas. *Appl. Catal. A* **2014**, *483*, 10-18.
- (25) Xiang, Y.; Barbosa, R.; Kruse, N. Higher Alcohols Through CO Hydrogenation over CoCu Catalysts: Influence of Precursor Activation. *ACS Catal.* **2014**, *4*, 2792-2800.
- (26) Nilekar, A. U.; Alayoglu, S.; Eichhorn, B.; Mavrikakis, M. Preferential CO Oxidation in Hydrogen: Reactivity of Core–Shell Nanoparticles. *J. Am. Chem. Soc.* **2010**, *132*, 7418-7428.
- (27) Subramanian, N. D.; Balaji, G.; Kumar, C. S. S. R.; Spivey, J. Development of Cobalt–Copper Nanoparticles as Catalysts for Higher Alcohol Synthesis from Syngas. *J. Catal. Today* **2009**, *147*, 100-106.
- (28) Alayoglu, S.; Beaumont, S. K.; Melaet, G.; Lindeman, A. E.; Musselwhite, N.; Brooks, C. J.; Somorjai, G. A. Surface Composition Changes of Redox Stabilized Bimetallic CoCu Nanoparticles Supported on Silica under H₂ and O₂ Atmospheres and During Reaction between CO₂ and H₂: In Situ X-ray Spectroscopic Characterization. *J. Phys. Chem. C* **2013**, *117*, 21803-21809.
- (29) Khodakov, A. Y.; Chu, W.; Fongarland, P. Advances in the Development of Novel Cobalt Fischer-Tropsch Catalysts for Synthesis of Long-Chain Hydrocarbons and Clean Fuels. *Chem. Rev.* **2007**, *107*, 1692-1744.
- (30) Spivey, J. J.; Egbebi, A. Heterogeneous Catalytic Synthesis of Ethanol from Biomass-Derived Syngas. *Chem. Soc. Rev.* **2007**, *36*, 1514-1528.
- (31) Gupta, M.; Smith, M. L.; Spivey, J. J. Heterogeneous Catalytic Conversion of Dry Syngas to Ethanol and Higher Alcohols on Cu-based Catalysts. *ACS Catal.* **2011**, *1*, 641-656.

- 1
2
3 (32) Waugh, K. C. Methanol Synthesis. *Catal. Today* **1992**, *15*, 51-75.
4
5
6 (33) Klier, K. Methanol Synthesis. *Adv. Catal.* **1982**, *31*, 243-313.
7
8 (34) Toyir, J.; de la Piscina, P. R.; Fierro, J. L. G.; Homs, N. Highly Effective Conversion of
9 CO₂ to Methanol over Supported and Promoted Copper-based Catalysts: Influence of
10 Support and Promoter. *Appl. Catal. B* **2001**, *29*, 207-215.
11
12
13 (35) Iablokov, V.; Beaumont, S. K.; Alayoglu, S.; Pushkarev, V. V.; Specht, C.; Gao, J.;
14 Somorjai, G. A. Size-Controlled Model Co Nanoparticle Catalysts for CO₂ Hydrogenation:
15 Synthesis, Characterization, and Catalytic Reactions. *Nano Lett.* **2012**, *12*, 3091-3096.
16
17
18 (36) Melaet, G., Ralston, W. T.; Li, C. S.; Alayoglu, S.; An, K.; Musselwhite, N.; Somorjai, G.
19 A. Evidence of Highly Active Cobalt Oxide Catalyst for the Fischer–Tropsch Synthesis
20 and CO₂ Hydrogenation. *J. Am. Chem. Soc.* **2014**, *136*, 2260-2263.
21
22
23 (37) Melaet, G.; Lindeman, A. E.; Somorjai, G. A. Cobalt Particle Size Effects in the Fischer–
24 Tropsch Synthesis and in the Hydrogenation of CO₂ Studied with Nanoparticle Model
25 Catalysts on Silica. *Top. Catal.* **2014**, *57*, 500-507.
26
27
28 (38) Wang, Z. J.; Skiles, S.; Yang, F.; Yan, Z.; Goodman, D. W. Particle Size Effects in
29 Fischer–Tropsch Synthesis by Cobalt. *Catal. Today* **2012**, *181*, 75-81.
30
31
32 (39) Tuxen, A.; Carenco, S.; Chintapalli, M.; Chuang, C. H.; Escudero, C.; Pach, E.; Salmeron,
33 M. Size-Dependent Dissociation of Carbon Monoxide on Cobalt Nanoparticles. *J. Am.*
34 *Chem. Soc.* **2013**, *135*, 2273-2278.
35
36
37 (40) Natesakhawat, S.; Lekse, J. W.; Baltrus, J. P.; Ohodnicki Jr, P. R.; Howard, B. H.; Deng,
38 X.; Matranga, C. Active Sites and Structure–Activity Relationships of Copper-Based
39 Catalysts for Carbon Dioxide Hydrogenation to Methanol. *ACS Catal.* **2012**, *2*, 1667-
40 1676.
41
42
43
44
45
46
47
48
49
50
51
52
53
54
55
56
57
58
59
60

- 1
2
3
4
5
6
7
8
9
10
11
12
13
14
15
16
17
18
19
20
21
22
23
24
25
26
27
28
29
30
31
32
33
34
35
36
37
38
39
40
41
42
43
44
45
46
47
48
49
50
51
52
53
54
55
56
57
58
59
60
- (41) Prieto, G.; Beijer, S.; Smith, M. L.; He, M.; Au, Y.; Wang, Z.; Bruce, D.A.; de Jong, K.P.; Spivey, J.J.; de Jongh, P. E. Design and Synthesis of Copper–Cobalt Catalysts for the Selective Conversion of Synthesis Gas to Ethanol and Higher Alcohols. *Angew. Chem., Int. Ed.* **2014**, *53*, 6397-6401.
- (42) Carenco, S.; Tuxen, A.; Chintapali, M.; Pach, E.; Escudero, C.; Ewers, T. D.; Jiang, P.; Borondics, F.; Thornton, G.; Alivastos, A. P.; Bluhm, H.; Guo, J.; Salmeron, M. Dealloying of Cobalt from CuCo Nanoparticles Under Syngas Exposure. *J. Phys. Chem. C* **2013**, *117*, 6259-6266.
- (43) Puentes, V. F.; Krishnan, K. M.; Alivisatos, A. P. Colloidal Nanocrystal Shape and Size Control: the Case of Cobalt. *Science* **2001**, *291*, 2115-2117.
- (44) Hung, L. I.; Tsung, C. K.; Huang, W.; Yang, P. Room-Temperature Formation of Hollow Cu₂O Nanoparticles. *Adv. Mater.* **2010**, *22*, 1910-1914.
- (45) Rioux, R. M.; Song, H.; Hoefelmeyer, J. D.; Yang, P.; Somorjai, G. A. High-Surface-Area Catalyst Design: Synthesis, Characterization, and Reaction Studies of Platinum Nanoparticles in Mesoporous SBA-15 Silica. *J. Phys. Chem. B* **2005**, *109*, 2192-2202.
- (46) Xia, X.; Wang, Y.; Ruditskiy, A.; Xia, Y. 25th Anniversary Article: Galvanic Replacement: A Simple and Versatile Route to Hollow Nanostructures with Tunable and Well-Controlled Properties. *Adv. Mater.* **2013**, *25*, 6313-6333.
- (47) Dinega, D. P.; Bawendi, M. G. A Solution-Phase Chemical Approach to a new Crystal Structure of Cobalt. *Angew. Chem., Int. Ed.* **1999**, *38*, 1788-1791.
- (48) ASM Handbook; Alloy Phase Diagrams. *ASM International: OH* **1992**; Vol.3.

- 1
2
3
4
5
6
7
8
9
10
11
12
13
14
15
16
17
18
19
20
21
22
23
24
25
26
27
28
29
30
31
32
33
34
35
36
37
38
39
40
41
42
43
44
45
46
47
48
49
50
51
52
53
54
55
56
57
58
59
60
- (49) Ahmed, J.; Ganguly, A.; Saha, S.; Gupta, G.; Trinh, P.; Mugweru, A. M.; Ganguli, A. K. Enhanced Electrocatalytic Activity of Copper–Cobalt Nanostructures. *J. Phys. Chem. C* **2011**, *115*, 14526-14533.
- (50) Li, G.; Wang, Q.; Li, D.; Lü, X.; He, J. Structure Evolution During the Cooling and Coalesced Cooling Processes of Cu–Co Bimetallic Clusters. *Phys. Lett. A* **2008**, *372*, 6764-6769.
- (51) de la Peña O'Shea, V. A.; Homs, N.; Pereira, E. B.; Nafria, R.; Ramírez de la Piscina, P. X-ray Diffraction Study of Co₃O₄ Activation Under Ethanol Steam-Reforming. *Catal. Today* **2007**, *126*, 148-152.
- (52) Khodakov, A. Y.; Lynch, J.; Bazin, D.; Rebours, B.; Zanier, N.; Moisson, B.; Chaumette, P. Reducibility of Cobalt Species in Silica-Supported Fischer–Tropsch Catalysts. *J. Catal.* **1997**, *168*, 16-25.
- (53) Smith, M. L.; Campos, A.; Spivey, J. J. Reduction Processes in Cu/SiO₂, Co/SiO₂, and CuCo/SiO₂ Catalysts. *Catal. Today* **2012**, *182*, 60-66.
- (54) Fierro, G.; Jacono, M. L.; Inversi, M.; Dragone, R.; Porta, P. TPR and XPS Study of Cobalt–Copper Mixed Oxide Catalysts: Evidence of a Strong Co–Cu Interaction. *Top. Catal.* **2000**, *10*, 39-48.
- (55) Deng, S.; Chu, W.; Xu, H.; Shi, L.; Huang, L. Effects of Impregnation Sequence on the Microstructure and Performances of Cu-Co Based Catalysts for the Synthesis of Higher Alcohols. *J. Nat. Gas Chem.* **2008**, *17*, 369-373.
- (56) Cesar, D. V.; Pérez, C. A.; Salim, V. M. M.; Schmal, M. Stability and Selectivity of Bimetallic Cu–Co/SiO₂ Catalysts for Cyclohexanol Dehydrogenation. *Appl. Catal. A* **1999**, *176*, 205-212.

- 1
2
3
4
5
6
7
8
9
10
11
12
13
14
15
16
17
18
19
20
21
22
23
24
25
26
27
28
29
30
31
32
33
34
35
36
37
38
39
40
41
42
43
44
45
46
47
48
49
50
51
52
53
54
55
56
57
58
59
60
- (57) Yin, Y.; Erdonmez, C. K.; Cabot, A.; Hughes, S.; Alivisatos, A. P. Colloidal Synthesis of Hollow Cobalt Sulfide Nanocrystals. *Adv. Funct. Mater.* **2006**, *16*, 1389-1399.
- (58) Ibáñez, M.; Fan, J.; Li, W.; Cadavid, D.; Nafria, R.; Carrete, A.; Cabot, A. Means and Limits of Control of the Shell Parameters in Hollow Nanoparticles Obtained by the Kirkendall Effect. *Chem. Mater.* **2011**, *23*, 3095-3104.
- (59) Cabot, A.; Ibáñez, M.; Guardia, P.; Alivisatos, A. P. Reaction regimes on the synthesis of hollow particles by the Kirkendall effect, *J. Am. Chem. Soc.* **2009**, *131*, 11326-11328.
- (60) Cabot, A.; Puentes, F. F.; Shevchenko, E.; Yin, Y.; Balcells, L.; Marcus, M. A.; Hughes, S. M.; Alivisatos, A. P.; Vacancy coalescence during oxidation of iron nanoparticles, *J. Am. Chem. Soc.* **2007**, *129*, 10358-10360.
- (61) Evans, J. W.; Wainwright, M. S.; Bridgewater, A. J.; Young, D. J. On the Determination of Copper Surface Area by Reaction with Nitrous Oxide. *Appl. Catal.* **1983**, *7*, 75-83.
- (62) Robinson, W. R. A. M.; Mol, J. C. Characterization and Catalytic Activity of Copper/Alumina Methanol Synthesis Catalysts. *Appl. Catal.* **1988**, *44*, 165-177.
- (63) Mahdavi, V.; Peyrovi, M. H. Synthesis of C₁-C₆ Alcohols Over Copper/Cobalt Catalysts: Investigation of the Influence of Preparative Procedures on the Activity and Selectivity of Cu-Co₂O₃/ZnO, Al₂O₃ Catalyst. *Catal. Commun.* **2006**, *7*, 542-549.
- (64) Lahtinen, J.; Anraku, T.; Somorjai, G. A. C, CO and CO₂ Hydrogenation on Cobalt Foil Model Catalysts: Evidence for the Need of CoO Reduction. *Catal. Lett.* **1994**, *25*, 241-255.
- (65) Sandoval, M. J.; Bell, A. T. Temperature-Programmed Desorption Studies of the Interactions of H₂, CO, and CO₂ with Cu/SiO₂. *J. Catal.* **1993**, *144*, 227-237.

- 1
2
3
4
5
6
7
8
9
10
11
12
13
14
15
16
17
18
19
20
21
22
23
24
25
26
27
28
29
30
31
32
33
34
35
36
37
38
39
40
41
42
43
44
45
46
47
48
49
50
51
52
53
54
55
56
57
58
59
60
- (66) Barbier, A.; Tuel, A.; Arcon, I.; Kodre, A.; Martin, G. A. Characterization and Catalytic Behavior of Co/SiO₂ Catalysts: Influence of Dispersion in the Fischer–Tropsch Reaction. *J. Catal.* **2001**, *200*, 106-116.
- (67) Weatherbee, G. D.; Bartholomew, C. H. Hydrogenation of CO₂ on Group VIII Metals: IV. Specific Activities and Selectivities of Silica-Supported Co, Fe, and Ru. *J. Catal.* **1984**, *87*, 352-362.
- (68) Fujitani, T.; Nakamura, I.; Uchijima, T.; Nakamura, J. The Kinetics and Mechanism of Methanol Synthesis by Hydrogenation of CO₂ over a Zn-deposited Cu (111) Surface. *Surf. Sci.* **1997**, *383*, 285-298.
- (69) Clancy, P.; Breen, J. P.; Ross, J. R. The Preparation and Properties of Coprecipitated Cu–Zr–Y and Cu–Zr–La Catalysts used for the Steam Reforming of Methanol. *Catal. Today* **2007**, *127*, 291-294.
- (70) Chinchin, G. C.; Waugh, K. C.; Whan, D. A. The Activity and State of the Copper Surface in Methanol Synthesis Catalysts. *Appl. Catal.* **1986**, *25*, 101-107.
- (71) Fujitani, T.; Nakamura, J. The Effect of ZnO in Methanol Synthesis Catalysts on Cu Dispersion and the Specific Activity. *Catal. Lett.* **1998**, *56*, 119-124.
- (72) Robbins, J. L.; Iglesia, E.; Kelkar, C. P.; DeRites, B. Methanol Synthesis over Cu/SiO₂ Catalysts. *Catal. Lett.* **1991**, *10*, 1-10.

Insert Table of Contents Graphic and Synopsis Here

